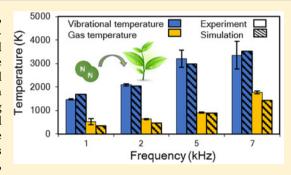# Power Pulsing To Maximize Vibrational Excitation Efficiency in N$_2$ Microwave Plasma: A Combined Experimental and Computational Study

S. Van Alphen,[†] V. Vermeiren,[†] T. Butterworth,[‡] D. C. M. van den Bekerom,[‡] G. J. van Rooij,[‡] and A. Bogaerts*,[†]

[†]Research Group PLASMANT, Department of Chemistry, University of Antwerp, 2610 Antwerp, Belgium
[‡]Dutch Institute for Fundamental Energy Research, 5600 HH Eindhoven, The Netherlands

S *Supporting Information*

ABSTRACT: Plasma is gaining increasing interest for N$_2$ fixation, being a flexible, electricity-driven alternative for the current conventional fossil fuel-based N$_2$ fixation processes. As the vibrational-induced dissociation of N$_2$ is found to be an energy-efficient pathway to acquire atomic N for the fixation processes, plasmas that are in vibrational nonequilibrium seem promising for this application. However, an important challenge in using nonequilibrium plasmas lies in preventing vibrational−translational (VT) relaxation processes, in which vibrational energy crucial for N$_2$ dissociation is lost to gas heating. We present here both experimental and modeling results for the vibrational and gas temperature in a microsecond-pulsed microwave (MW) N$_2$ plasma, showing how power pulsing can suppress this unfavorable VT relaxation and achieve a maximal vibrational nonequilibrium. By means of our kinetic model, we demonstrate that pulsed plasmas take advantage of the long time scale on which VT processes occur, yielding a very pronounced nonequilibrium over the whole N$_2$ vibrational ladder. Additionally, the effect of pulse parameters like the pulse frequency and pulse width are investigated, demonstrating that the advantage of pulsing to inhibit VT relaxation diminishes for high pulse frequencies (around 7000 kHz) and long power pulses (above 400 μs). Nevertheless, all regimes studied here demonstrate a clear vibrational nonequilibrium while only requiring a limited power-on time, and thus, we may conclude that a pulsed plasma seems very interesting for energy-efficient vibrational excitation.

1. INTRODUCTION

Nitrogen (N) is a crucial element, being a major building block for proteins, nucleic acids and other cellular constituents, responsible for life on Earth. On Earth we are surrounded by this vital element, as almost 79% of the Earth's atmosphere consists of molecular nitrogen gas (N$_2$). However, this abundant nitrogen source is not available to the majority of living organisms, as the molecule's strong triple bond and very stable electronic configuration prevent organisms to easily incorporate it in any biosynthetic pathway. Our agricultural system, and life on Earth in general, thus depends on N$_2$ fixation processes that convert N$_2$ into simple nitrogen compounds, such as ammonia (NH$_3$) or nitric oxides (NO$_x$), which in turn can be further used as precursors for the synthesis of more complex molecules.[1]

Nature displays a few methods of N$_2$ fixation, as it occurs spontaneously on Earth by specialized N$_2$ fixing microorganisms or by the high energy present in a lightning strike.[2] However, the increased global population has intensified agriculture past the point that this amount of biologically fixed N$_2$ is sufficient for raising the required food crops. This issue led in 1908 to the development of the Haber−Bosch process,

for the synthesis of NH$_3$ out of N$_2$ and H$_2$, which to this day remains the conventional standard for industrial N$_2$ fixation.[3] Today the Haber−Bosch process produces more than 130 million tons of NH$_3$ per year, indirectly feeding 40% of the world population through fertilizer production.[1] Unfortunately, the process consumes almost 2% of the world's total energy production through fossil fuel consumption associated with the H$_2$ production step. Additionally, this energy intensive step emits 300 million metric tons of CO$_2$ each year.[4,5] As major environmental concerns associated with fossil fuels require a short-term transition from a carbon-based energy economy to a sustainable one, energy intensive chemical processes like the Haber−Bosch process are detrimental in our present-day society. The Haber−Bosch process was significantly optimized the past 100 years, essentially reaching its theoretical optimization limits (0.48 MJ/mol NH$_3$).[2,3] As a result, the environmental impact of N$_2$ fixation processes can only be

improved by considering new, innovative approaches, which are very different from the Haber−Bosch process.[6,7]

Among several solutions, such as electrolysis, biological nitrogen fixation, and catalytic conversion under ambient pressure, the use of nonequilibrium plasmas seems very promising.[8] Nonequilibrium plasmas enable high energy electrons to forcefully interact with the stable N≡N bond, while the bulk gas can remain close to room temperature. This electricity-driven, and thus in principle fossil fuel-free solution harmonizes greatly with a future of renewal energy from wind and solar cells.[9] Furthermore, the theoretical energy consumption limit of the plasma-based NO_x production process is 2.5 times lower than that of the Haber−Bosch process, giving it an edge over the classical process when it is optimized toward this limit.[10]

The plasma-based N_2 fixation process has already been tested in different kind of plasma reactors,[11] for both NH_3 synthesis from H_2 and N_2[12−21] and NO_x synthesis from O_2 and N_2.[9,21−36] The most promising results were delivered for NO_x production in a microwave (MW) reactor at reduced pressure, yielding an energy cost of 0.3 MJ/mol for a NO_x yield of 14%.[10] Second place is a gliding arc (GA) reactor, with a 2% NO_x yield and 2.8 MJ/mol energy consumption, reached at atmospheric pressure.[37] These reactors are known to create significant vibrational excitation of N_2. Indeed, as revealed by recent computer modeling, an efficient way of breaking the N≡N bond is not achieved by direct electronic excitation with high energy electrons but by gradually exciting the vibrational states of N_2.[8] These vibrationally excited N_2 molecules collide with each other, inducing vibrational-vibrational (VV) relaxation in which they exchange their vibrational energy. Going through a series of these VV relaxation collisions, molecules can gradually populate higher vibrational energy levels, a process which is often referred to as vibrational ladder climbing.[8,37−39] Through this vibrational ladder climbing, a N_2 molecule eventually reaches energy levels close to the bond dissociation energy of the N≡N bond (9.765 eV), facilitating the breakage of the bond.

However, vibrationally excited N_2 molecules can relax back to lower vibrational levels via vibrational−translational (VT) relaxation.[38,40] This relaxation process causes the energy of N_2 to be transferred from vibrational to translational energy upon collision with a ground state N_2 molecule or another species. This is unfavorable, as the vibrational energy, which is required to overcome the dissociation energy barrier, is lost to gas heating. Furthermore, this energy loss mechanism becomes more important at high gas temperature, creating a self-accelerating mechanism.[8] Avoiding the temperature rise and the thermalization of the vibrational energy is thus a priority in N_2 fixation through nonequilibrium plasmas.[40]

One option to prevent the gas temperature from raising too high includes operating in a supersonic gas flow, as was demonstrated for CO_2 MW plasmas.[41,42] As a gas uses its own internal energy to accelerate supersonically, the gas cools itself, avoiding thermalization of the vibrational and translational levels. Another option exists in pulsing the power source of the plasma, so that time is provided for the plasma to cool down between pulses.[11,43] This last option is relatively easy to apply on a plasma setup and has been explored for CO_2 MW plasmas[44−46] but not yet for N_2 plasmas. Although it seems promising for N_2 fixation as well, the influence of power pulsing on the actual plasma processes and chemistry lacks a fundamental understanding to fully predict its advantages.

Indeed, the exact behavior of the nonequilibrium between vibrational and thermal energy in a pulsed plasma is not yet well understood, as the effect of pulsing on vibrational mechanisms, like VT and VV relaxation, is not readily available in experiments.

The aim of this research is to address these fundamentals of the vibrational excitation mechanism of N_2 in a pulsed plasma, by a combined experimental and computational study of a pulsed N_2 MW plasma. Combined experimental and computational studies have already proven to deliver satisfactory result in the past, as they have established the state of the art for the vibrational kinetics of N_2 plasmas. A study based on coherent anti-Stokes Raman (CARS) by Massabieaux et al.,[47] supported by modeling results by Capitelli et al.,[48] as well as cavity ringdown spectroscopy measurements by Macko et al.,[49] supported by simulations of Guerra et al.,[50] has provided important insights in the vibrational kinetics of low pressure DC N_2 discharges, identifying the role of superelastic vibrational collisions and VV relaxation in determining the electron energy and vibrational energy distribution. In our research, we applied the same approach to identify the vibrational kinetics of pulsed MW systems.

Specifically, we want to examine if power pulsing can enhance the vibrational nonequilibrium by reducing the gas temperature and consequent VT relaxation, as well as how the nonequilibrium changes when important pulse parameters like the pulse frequency and pulse width are changed. The vibrational nonequilibrium will both be measured experimentally and calculated with a detailed chemical kinetics model, for different pulse regimes with varying pulse frequencies and pulse widths. In addition, the modeling will reveal the vibrational mechanism and chemistry occurring in the nonequilibrium plasma, which cannot be observed experimentally.

2. EXPERIMENTAL DETAILS

2.1. Vibrational Nonequilibrium. To observe the effect of pulsed power on the vibrational nonequilibrium, we first need to quantify this nonequilibrium. In nonequilibrium conditions, each degree of freedom is represented by a unique temperature, meaning that besides the gas temperature (T_{gas}), representing the translational degree of freedom, two new temperatures are defined, i.e. the vibrational temperature (T_v) and rotational temperature (T_r). Together, T_v, T_r and T_{gas} represent to which extent the energy is distributed unequally between these degrees of freedom and thus serve as a quantification for the existing vibrational nonequilibrium. Although vibrational states up to level 8 can be measured for some conditions, limited signal-to-noise occasionally prevents the detection of the higher levels. In order to consistently compare the simulations with experimental data at all conditions, a vibrational temperature T_v is defined based on the energy and the population density of the first vibrational level (E_1 and n_1) and the population of the vibrational ground state (n_0):

$$T_v = \frac{E_1}{k_b \ln\left(\frac{n_1}{n_0}\right)}$$

(1)

It should be noted that having a definition that is compatible with every experimental condition comes at the price of not being able to compare the particular shape of the VDF—in particular, deviations from a Boltzmann distribution. While the
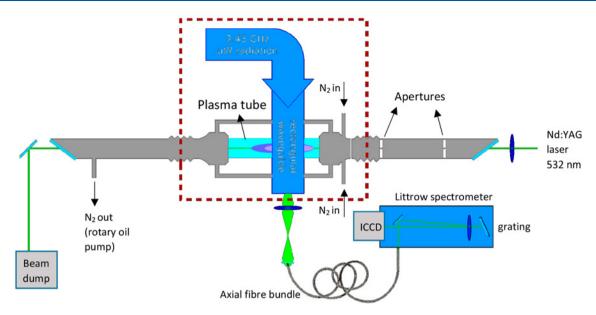
Figure 1. Schematic overview of the Raman scattering setup, installed at the MW setup (highlighted by the dashed red box).

comparison of simulated and experimentally obtained T_v is presented in section 4.1.a, a comparison between the fully detailed VDF's are presented in section 4.1.c) for warranting conditions. As the aim of this study is to achieve vibrational nonequilibrium in MW plasma, T_v is of special interest. T_r on the other hand, is assumed to be in equilibrium with the translational temperature at all times due to fast translational relaxation (less than nanosecond time scale), allowing us to use T_r as a good estimation for T_{gas}.[51]

2.2. Vibrational Raman Spectroscopy. Laser spontaneous Raman scattering is the diagnostic of choice to determine T_v and T_r ($=T_{gas}$) and thus to characterize the translational−vibrational nonequilibrium. This spectroscopic technique observes Raman scattering, which is an inelastic process, in which energy transfer takes place between the scattered light and the molecule. In this process an incident photon is momentarily absorbed by a transition from the ground state into a virtual state. Subsequently, a new photon is created and scattered by relaxing from this virtual state. The most probable transition from the virtual state is back to the ground state, resulting in no change in energy (elastic or Rayleigh scattering). However, the event can occur (approximately 1 in 10 million) in which the transition from the virtual state occurs to a vibrationally or rotationally excited state of the molecule. This results in an energy transfer between the molecule and the scattered photon and is described as inelastic scattering or Raman scattering. As the incident light either gains or loses a discrete amount of energy proportional to the change in vibrational (ν) and/or rotational (J) quantum number during the scattering process, analyzing the energy of an inelastically scattered photon directly yields information about the rotational and vibrational state of a molecule.

Considering only the Stokes signals ($\Delta\nu = +1$) of a spectrum, which are the most intense, every excited ro-vibrational state will be represented by a Raman signal at one distinct wavelength. The intensity of this signal is proportional to the population density of the ro-vibrational state. The number density ($n_{\nu,J}$) of a ro-vibrational state (at vibrational level ν and rotational level J) is given by[52]

$$n_{v,J} = n_0 \frac{\left(\exp -\frac{hcG(v)}{kT_{vib}}\right)}{Q_{vib}(T_{vib})} \frac{g_J \exp\left(-\frac{hcF_v(J)}{kT_{rot}}\right)}{Q_{rot}(T_{rot})} \quad (2)$$

where $G(v) = \omega\left(v + \frac{1}{2}\right)$ is the vibrational energy (harmonic approximation), $F_v(J) = B_v J(J + 1)$ is the rotational energy (rigid rotor approximation), $g_J = 2J + 1$ the degeneracy of the rotational state, B_v the rotational constant of N_2, $Q_{vib} = \frac{1}{1 - \exp\left(-\frac{hcG(0)}{kT_{vib}}\right)}$ the vibrational partition function and $Q_{rot} = \frac{kT_{rot}}{hcB}$ the rotational partition function.

The Raman shift in the spectrum is then given by[52]

$$\Delta\nu = G(v') + F_v(J') - (G(v'') + F_{v''}(J'')) \quad (3)$$

where $G(v')$ and (v'') are the vibrational energy of the upper and lower state, respectively, and $F_v(J')$ and $F_{v''}(J'')$ are the rotational energy of the upper and lower state, respectively.

In a single Raman signal, three ro-vibrational branches can be identified: O($\Delta J = +2$), Q($\Delta J = 0$) and S($\Delta J = -2$). Since the O and S branches are orders of magnitudes less intense than the Q branch, only the Q branches are resolved.[52]

To extract T_v and T_{gas} out of a Raman spectrum, the Raman signals are fitted following the method of Gatti et al.,[53] describing the intensity of the scattered light as

$$I = (v_i, J, T_r)$$
$$= CN\gamma_{V_i}(\nu_l - |\Delta\nu(v_i, J)|)^4 \exp\left(-\frac{hcB_{v_i}J(j + 1)}{kT_r}\right) \quad (4)$$

where C is a factor accounting for the overall collection efficiency of the diagnostics, N is the scatterer's number density, T_r is the rotational temperature, ν_l is the wavenumber of the incident laser radiation, $\Delta\nu(V_i, J)$ is the energy shift associated with the transition, and B_{Vi} and γ_{Vi} are the rotational constant and the polarizability of a molecule in the vibrational state V_i, respectively. For nondegenerate fundamental bands, the Raman shift for a given rotational quantum number J is equal to

$$|\Delta\nu(V_i, J)| \cong \nu_{vib} + (B_{V_{i+1}} - B_{V_i})J(J + 1) \qquad (5)$$

where ν_{vib} is the energy difference between the two vibrational levels involved in the transition.

As shown in eq 4, the profile of a band is a function of T_{rot}. Indeed, T_{rot} ($=T_{gas}$) defines the rotational fine structure of a Q branch and thus the overall shape of the peak in the Raman spectrum.[54] The value for T_{gas} thus results from fitting eq 4 to the different bands in the spectra, the other fitting parameter being the height of the peak. In this fit T_{gas} is considered to be constant, regardless of the vibrational state. Each Q branch, after being calculated with the fitted heights and T_{gas}, is integrated to obtain a value proportional to the population of each vibrational level and to the collection efficiency of the apparatus. The relative (to ground state) populations are then calculated using

$$\frac{N_\nu}{N_0} = \frac{1}{\nu + 1}\frac{\int I_\nu(\overline{\nu})\,\mathrm{d}\overline{\nu}}{\int I_0(\overline{\nu})\,\mathrm{d}\overline{\nu}} \qquad (6)$$

where N_0 and N_ν are the populations of the ground state and a vibrational level, respectively, and the integrals are calculated over the fitted Q branches. In eq 6, the $(\nu + 1)$ factor corrects for the dependence of the Raman scattering cross section on the vibrational quantum number. In conclusion, the fit outcomes are (1) the rotational temperature, T_r, and (2) the relative populations of the vibrational levels, which in turn allow to calculate T_v via eq 1. The upper limit of the detectable vibrational levels was dictated by the spectral window of the spectrometer. Higher vibrational levels could technically be measured using the same system if a grating with a lower dispersion were used. For much higher levels, more sensitive techniques like cavity ringdown spectroscopy (CRDS) may be necessary,[49] which would lose the advantage of measuring all detected vibrational levels at the same time. Another technique that is often used is coherent antistokes Raman spectroscopy (CARS),[47] but given the relatively low pressure and high vibrational temperature of the system, the limited advantage of CARS over spontaneous Raman scattering may not justify the added experimental complexity.

2.3. Experimental Setup. The experiments are conducted in a MW plasma reactor, as described by van den Bekerom et al.,[55] depicted schematically in Figure 1. In this flow reactor, the plasma is generated in a 26 mm outer diameter quartz tube (plasma tube in Figure 1). This tube is supplied with 4 slm of N_2 gas through two tangential injection nozzles, creating rotation in the flow and stabilizing the plasma in the center of the plasma tube. After passing through the plasma tube, gas is exhausted by a scroll pump, keeping the gas pressure in the tube at 25 mbar. The plasma in the quartz tube is generated by applying 2.45 GHz microwave radiation to the gas through a rectangular WR-340 waveguide perpendicular to the plasma tube. A movable plunger positioned at a quarter wavelength distance from the center of the tube creates a cavity that sustains a standing wave of MW radiation. Three stub tuners inserted into the waveguide allow the impedance of the microwaves to be tuned to match the plasma impedance and form a stable plasma.

The MW power is applied in pulses. The signals triggering the MW source in a pulsed manner are provided by a signal generator (Rigol LX1 2 channel DG1602Z). The generator sends periodic signals with a frequency of choice to the synthesizer of the MW source, which transforms the signal into

four MW channels, each transporting ±150 W of MW power. The waves in these channels are passed to the amplifier, which amplifies the microwaves by means of coaxial cables and eventually sends them to the waveguide.

The diagnostics are provided by a frequency doubled Nd:YAG laser (6W, 532 nm) focused axially into the center of the plasma using a 1700 mm focal length lens. The flash lamp as well as the Q-switch of the laser are triggered by the previously mentioned Rigol LX1 signal generator, firing the laser at a frequency of 10 Hz. The beam passes through two apertures, so stray light is reduced. Scattered light in the plasma region is collected perpendicular to the beam path through a hole in the waveguide using an axial fiber bundle. Light is focused on the bundle using a 100 mm focal length lens, equipped with a 550 nm AR long-pass filter to further reduce stray light. The bundle projects the collected light into a custom Littrow spectrometer, equipped with an emICCD camera (PI-MAX4:1024i) that accumulates over 9000 shots during one experiment. These camera shots are also triggered by the previously mentioned signal generator. A delay generator (Stanford Instruments DG645 4 channel digital delay/pulse generator) manages the delay between all the trigger signals of the signal generator, so the firing of the laser, the imaging of the camera, and the MW pulses are always synchronized.

3. COMPUTATIONAL DETAILS

3.1. Equations Solved by the Model. While very valuable information about the vibrational and gas temperature arises from the Raman experiments, they do not allow a direct analysis of the plasma parameters, important reactions, or vibrational mechanisms that led to these temperatures. Furthermore, no information is delivered about the high vibration levels, as their low intensity peaks are not detectable by the Raman setup. To acquire this kind of information, the experimental results are backed up by a 0D chemical kinetics model. To simulate the experimental MW setup, we use the 0D model ZDPlasKin (Zero-Dimensional Plasma Kinetics solver).[56] In this model the time evolution of the plasma species densities is calculated by balance equations, taking into account the various production and loss terms by chemical reactions:

$$\frac{\mathrm{d}n_i}{\mathrm{d}t} = \sum_j \left[(a_{ij}^R - a_{ij}^L)k_j \prod_l n_l^L\right] \qquad (7)$$

Here, n_i is the density of species i and a_{ij}^R and a_{ij}^L are the stoichiometric coefficients of species i on the right-hand and left-hand side of the reaction j. n_l is the density of the reacting species l. k_j is the reaction rate constant of reaction j, which has the general form:

$$a_A A + a_B B (+\Delta H) \xrightarrow{k_j} a_C C + a_D D (+\Delta H) \qquad (8)$$

In which A, B, C, and D are the species and a_A, a_B, a_C, and a_D their stoichiometric coefficients. ΔH represents the possible energy change during the reaction, used to calculate the gas temperature self-consistently as the reactions progress. The rate coefficients of these reactions are adopted from literature for the heavy particle reactions, whereas the rate coefficients for the electron impact reactions are calculated with a Boltzmann solver, BOLSIG+,[57] built in ZDPlasKin. This Boltzmann routine solves the Boltzmann equation for the

electrons using a two-term approximation, calculating the electron energy distribution function (EEDF). From the EEDF the mean electron energy and the different electron impact rate, coefficients are obtained through the following equation:

$$k_j = \int_0^{+\infty} \sigma_j(\varepsilon) f_e(\varepsilon) \sqrt{\frac{2\varepsilon}{m_e}} \, d\varepsilon \tag{9}$$

Here ε represents the electron energy, $\sigma_j(\varepsilon)$ the cross section of the jth electron collision reaction, $f_e(\varepsilon)$ the EEDF, and m_e the electron mass. The reaction cross sections $\sigma_j(\varepsilon)$ of the different elastic and inelastic collisions are adopted from the literature.[58,59] We included a complete set of cross sections interconnecting all 43 vibrational energy levels through single- and multiquantum transitions, as well as superelastic collisions, similar to the work of Colonna et al.[60] Indeed, Colonna et al. emphasized the role of superelastic collisions in structuring the EEDF, because during these collisions energy is transferred back from the heavy particles to the electrons. These collisions were found to be especially important in postdischarge conditions, where the average electron energy decreases, which is very relevant for the microsecond pulsed regimes that we study in this work. Indeed, both in the afterglow of the plasma, as well as in between pulses, no power is applied for several hundreds of microseconds, which are exactly the conditions in which superelastic collisions are responsible for shaping the EEDF. Colonna et al. also demonstrated the importance of the use of complete sets of cross sections that interconnect all vibrational levels, as recently calculated by Laporta et al.[60] It is demonstrated that these kind of cross section sets, based on internally consistent vibrational excitation calculations, provide more accurate results than scaling laws that are commonly used to cover the whole vibrational ladder.

Although eq 7 only solves the species densities as a function of time, the time dependence of the model is converted to an axial variation of the plasma quantities by following a volume element moving through the cylindrical plasma tube, by means of the gas flow rate, hence resulting in a quasi-1D model. The considered volume, which is always considered radially homogeneous in a 0D model, thus moves at a linear velocity v (as depicted in Figure 2):

$$v = \frac{Q_m}{\rho A} \tag{10}$$

Here Q_m is the mass flow rate, $A = \pi R^2$ is the tube cross section area and $\rho = \sum n_i M_i$ is the gas mass density. n_i is the number density of species i, and M_i is the mass of species i, while R is the tube radius.

By converting the time dependence of the 0D model into an axial dependence throughout the plasma tube, it is possible to express the power deposition as a function of the axial coordinate, z (see Figure 2). The effective power deposition in the plasma is depicted as the red pulses in Figure 2. From the applied power, the power density P is obtained through $=\frac{P_{applied}}{V}$, with V being the (cylindrical) plasma volume. The power density is used to calculate the reduced electric field, which is the ratio of electric field over gas number density (E/n), i.e., a very important plasma parameter, responsible for accelerating the electrons:
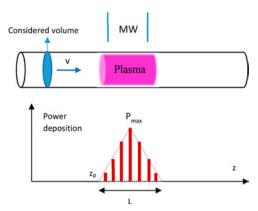

Figure 2. Schematic overview of the setup and power deposition profile used in the 0D (or quasi-1D) model. The plasma is formed between position z_p and position $z_p + L$. P_{max} is the maximum applied power at the center of the plasma.

$$\frac{E}{n} = \frac{\sqrt{P/\sigma}}{n} \tag{11}$$

Here σ is the plasma conductivity, which is estimated using the E/n value of the previous calculation iteration.

As we are particularly interested in the temperature evolution in the plasma, the gas temperature T_{gas} is calculated self-consistently at all times by

$$N \frac{\gamma k_B}{\gamma - 1} \frac{dT_{gas}}{dt} = P_{el} - \sum_j R_j \Delta H_j - \frac{8\lambda}{R^2}(T_g - T_w) \tag{12}$$

where $\gamma = \frac{C_p}{C_v}$ is the specific heat ratio (i.e., the ratio of the isobaric and isochoric heat capacity), k_B is the Boltzmann constant, P_{el} is the power density transferred from the electrons to the heavy particles through elastic collisions, R_j is the rate and ΔH_j is the enthalpy of reaction j, λ is the gas thermal conductivity (as a function of temperature; data taken from ref 61), and T_w is the wall temperature (assumed to be 300 K). The following plasma processes contribute most to the $R_j \Delta H_j$ term in eq 12 (by decreasing order of importance):

- VV relaxation: As the energy difference between consecutive levels decreases when going up the vibrational ladder, energy transfer between vibrational levels either releases or requires additional energy. VV relaxation reactions therefore exhibit both high negative as well as high positive ΔH_j values.
- Cooling upon collision with the wall.
- Dissociation/recombination, in which either energy is required or released to the gas, respectively.
- VT relaxation: This process predominantly heats the gas, especially from the high vibrational levels, which display a high VT relaxation rate.

To accurately simulate the experimental setup, the experimental parameters are used as direct input for the model, i.e., a pressure of 25 mbar and a flow rate of 4 slm. The experimental power density is also used as input in the model. As it depends on the deposited power and the plasma volume, both the power deposition and the shape of the plasma are measured. The MW power is monitored through a diode in the waveguide, which measures the reflected MW power and subtracts it from the originally deposited power. The shape of the plasma and the plasma volume are investigated through

separate imaging experiments, for which more information can be found in the Supporting Information (section S.2).

3.2. Chemistry Set. The 0D chemical kinetics model contains 58 different plasma species (shown in Table 1),

Table 1. Species Included in the Model[a]

ground state species
N_2, N
vibrationally excited species
N_2(V1−V43)
electronically excited species
N_2 ($A^3\Sigma_u^+$), N_2 ($B^3\Pi_g$), N_2 ($W^3\Delta_u$), N_2 ($B'^3\Sigma_u$), N_2 ($C^3\Pi_u$), N_2 ($E^3\Sigma_g^+$), N_2 ($a'^1\Sigma_u^-$), N_2 ($a^1\Pi g$), N_2 ($a''^1\Sigma_g^+$), N_2 ($w^1\Delta_u$), N (2D), N (2P)
ions
N_2^+

[a]The notations of the electronically excited species are adopted from ref 62.

including N_2 ground state molecules, N atoms, N_2^+ ions, and several electronically excited N_2 molecules and N atoms. As we are interested in the vibrational ladder climbing mechanism of plasma-based N_2 fixation, 43 vibrational energy levels up to the dissociation limit of N_2 are included in the model as well. All these plasma species take part in 4000+ reactions, including: electron impact reactions, various ion and neutral reactions, VT relaxation, VV relaxation, as well as dissociation from the N_2 ground state and the various vibrational levels. They are listed in the Supporting Information (section S.2).

3.3. Model Assumptions and Sensitivity Analysis. A major part of this study relies on kinetic modeling results, explaining the plasma processes that lead to the experimentally observed temperatures. As we need to describe a detailed plasma chemistry, including many excited states, we need to use a 0D model, to avoid excessive calculation time. However, a 0D model naturally considers several assumptions and approximations, which will inevitably result in discrepancies with the experiments. To critically compare the 0D model results with the experimental data, it is important to identify the approximations of the model that could be causing these discrepancies, and discuss how changing them could improve the agreement between model and experiment. To identify

these aspects, a sensitivity analysis of the two most critical assumptions is made in the Supporting Information (section S.3) from which the conclusion is presented here. Only the physical limitation of the 0D model are discussed, as the FHO theory, on which the chemistry in the model is based, is considered and proven to be one of the most reliable source for vibrational kinetics of diatomic molecules.[63]

3.3.a. The Radial Gas Temperature Profile. A 0D model describes the plasma as a radially uniform cylinder-shaped volume, so all calculation results are radial averages over this cylinder-shaped volume. This is especially important for the calculation of the gas temperature, since both heat loss near the wall and gas heating inside the plasma are averaged out over the whole volume. The Raman experiments, however, measure the gas temperature only in the center of the plasma, as the laser of the Raman setup is focused in the center of the plasma tube. To compare the 0D calculation results with the experiments, we thus need to convert the radially averaged 0D gas temperature to the (generally hotter) gas temperature in the center. This conversion needs to be done by assuming a certain radial temperature profile in the plasma tube. From the sensitivity analysis in the Supporting Information (section S.3), it follows that the choice of this temperature profile is of vital importance for comparison with the experiments. Furthermore, the sensitivity analysis shows that a Gaussian temperature profile represents the most realistic situation, as the tangential gas inlets generate a vortex flow that captures the gas in the center of the tube. The width of the Gaussian temperature profile at each time is based on the width of the plasma.

3.3.b. Power Density Estimation. Another important assumption in the 0D model is the value of the power density used as input for the calculation of the reduced electric field in the model. As described in the Supporting Information (section S.2), the power density is calculated by measuring the absorbed MW power in the plasma and estimating the plasma volume from the plasma images in Figure S1. In the sensitivity analysis the power density is also shown to have a significant impact on the model results. However, the current estimation of the power density is proven to be reasonable, as the case of a 20% lower or higher power density delivers significantly worse agreement with the experiment than the current estimation.
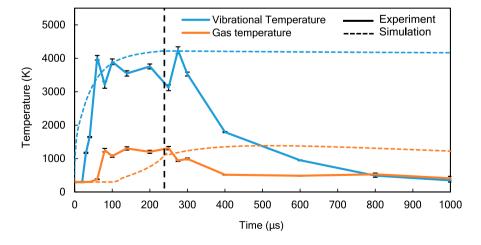

Figure 3. Time-evolution of the measured (full lines) and calculated (dashed lines) vibrational and gas temperature through a 233 μs pulse. The error bars of the experimental values are the errors resulting from the fitting procedure. The measured values are obtained in the center of the plasma. The end of the pulse is indicated with a vertical dashed line.

4. RESULTS AND DISCUSSION

4.1. Vibrational Nonequilibrium in an Isolated Pulse.

4.1.a. Vibrational and Gas Temperature. To establish the fundamental dynamics of vibrational excitation in a pulsed MW plasma, we first study the excitation process when an isolated pulse is applied. This single pulse experiment will capture the behavior of the vibrational and gas temperature on a μs time scale when a power pulse is applied. This single pulse plasma is experimentally achieved by pulsing at a low frequency (30 Hz), and using a high gas flow rate of 4 slm, so that no gas molecule will see more than one pulse when passing through the plasma tube. To obtain Raman signals of sufficient intensity, the scattered light is then collected over many of these single pulses. The duration of the pulse is chosen to be 233 μs, while the pressure is kept at 25 mbar. The time-evolution of the measured vibrational and rotational (gas) temperature through the pulse, in the center of the plasma, is plotted in Figure 3 (full lines), as obtained from Raman spectroscopy at different time frames in the 233 μs pulse. As light over a series of pulses was captured to create the data points in Figure 3, this figure represents an average of many pulses. The Raman spectra from which this information is extracted are added to the Supporting Information. A strong nonequilibrium is reached between the vibrational and gas temperature: Starting both at room temperature at the beginning of the pulse, the vibrational temperature quickly reaches values up to 4000 K at 60 μs, while the gas temperature plateaus at around 1000 K at 100 μs.

This strong nonequilibrium also follows from the 0D model. Indeed, the calculated vibrational and gas temperature profiles in the single pulse plasma, represented by the dashed lines in Figure 3, demonstrate a similar trend as observed in the experiments, i.e., a fast rising vibrational temperature and a much slower rising gas temperature. During the pulse both the calculated gas and vibrational temperature are in reasonable agreement with the experiments. The 0D model predicts the gas temperature to raise ± 100 μs later than experimentally observed, but he same absolute value is eventually reached. These discrepancies are discussed in the Supporting Information, where a sensitivity analysis of the most important assumptions of the model is presented. This analysis shows that the estimation of the power density and assumptions about the radial gas temperature profile are important for achieving satisfactory agreement with the experiment. After the pulse, a more significant discrepancy occurs. Whereas the experiments show a fast relaxation of both vibrational and gas temperature upon pulse termination, the model predicts a very slow relaxation of both temperatures. However, such a fast simultaneous relaxation of both temperatures is unlikely the result of solely collisional kinetics: At a pressure of 25 mbar, both the relaxation of the vibrational temperature as well as heat loss through collisions with the wall (for which the rates are displayed in section 1 of the Supporting Information) occur on a time scale that is too long (± 1 s time scale) to cool a vibrational temperature of 4000 K and gas temperature of 1000 K both to 300 K in only 500 μs. This indicates that physical transport processes like convection might either transport plasma particles away from the center, or mix cold untreated particles into the center when the plasma extinguishes, rather than actual chemical processes. Because of the 0D nature of the model, transport processes cannot be implemented in a straightforward way, suggesting a higher

dimensional model would be needed to fully describe the experimental result. However, for this kind of model, it would not be computationally feasible to describe the chemistry and vibrational processes of all 43 vibrational energy levels in depth, which is exactly the aim of this study.

4.1.b. Underlying Mechanisms. An explanation for the observed nonequilibrium in this single pulse is provided by calculating the time-integrated reaction rates of the three most important vibrational excitation and relaxation processes in the plasma, obtained from the model and shown in Table 2, i.e.,

Table 2. Time-Integrated Reaction Rates of the Three Major Vibrational Mechanisms Inside the one Pulse Plasma (233 μs), i.e., Electron Impact Vibrational Excitation, VV Relaxation, and VT Relaxation, Summed for all 43 Vibrational Levels and Multiplied with the Energy Difference of the Transitions, as Well as the Characteristic Time Scales of the Three Processes, at the Experimental Conditions under Study (1000 K, 25 mbar)

reaction type	time-integrated reaction rate (cm^{-3}) $\times \Delta E$ (eV)	characteristic time scale (s)
electron impact vibrational excitation	1.935×10^{21}	5.71×10^{-5}
VV relaxation	3.263×10^{20}	1.49×10^{-4}
VT relaxation	-1.159×10^{15}	0.618

electron impact vibrational excitation, VV relaxation, and VT relaxation. For each of these processes, the rates are summed over all 43 vibrational levels and multiplied with the energy difference of the transitions. This multiplication is done to indicate how much the three reactions distribute the applied energy over the whole vibrational ladder (i.e., up or down the ladder, for positive or negative values, respectively). Time-integration is performed over the pulse (233 μs).

The obtained values of these three major vibrational processes explain the experimental results: Electron impact vibrational excitation and VV relaxation, which stimulate the population of the (higher) vibrational levels, exhibit significantly higher reaction rates (multiplied with the energy differences) than VT relaxation, which is detrimental for populating the higher vibrational energy levels (hence, explaining the negative value) and causes gas heating. This difference of 5−6 orders of magnitude is responsible for the excessive vibrational population of higher vibrational levels and the limited gas heating in the plasma.

This significant difference between the three rates in a single plasma pulse can be explained by the time scale on which these processes occur. The time scales of electron impact vibrational excitation, VV relaxation, and VT relaxation can be represented by the characteristic time scales of the following reactions:

$e^- + N_2 \rightarrow e^- + N_2(V1)$, as characteristic electron impact vibrational excitation;

$N_2 + N_2(V1) \rightarrow N_2(V1) + N_2$, as characteristic VV relaxation;

$N_2 + N_2(V1) \rightarrow N_2 + N_2$, as characteristic VT relaxation, which are defined as

$$\tau_{e-V} = (n_e k_{1\rightarrow0}^{e-V})^{-1} \tag{13}$$

$$\tau_{VV} = (n_{N_2} k_{0\rightarrow1}^{1\rightarrow0})^{-1} \tag{14}$$

$$\tau_{VT} = (n_{N_2} k_{1\rightarrow0})^{-1} \tag{15}$$

with $k_{1\to0}^{e-V}$, $k_{1\to0}$ and $k_{0\to1}^{1\to0}$, the rate constants for the characteristic electron impact vibrational excitation, VT and VV relaxation reactions, respectively, n_e the electron density, and n_{N_2} the N_2 number density. Calculating these characteristic times for the experimental gas temperature and pressure (1000 K, 25 mbar), with the rate constants used in the model (taken from Table S2 of the Supporting Information) and the electron density calculated by the model, yields the characteristic time scales listed also in Table 2.

These characteristic reaction times reveal that electron impact vibrational excitation operates on the shortest time scale, closely followed by VV relaxation, while VT relaxation operates on a much longer time scale. This order indicates that reactions operating on a short time scale occur at a high rate in the plasma pulse. Indeed, because of their short reaction time scale, processes like electron impact vibrational excitation and VV relaxation already become significant very early in the plasma pulse; hence, they display a high reaction rate when integrated over the pulse time. It has to be noted, however, that only the characteristic time scales of VV and VT relaxation are directly comparable. Indeed, they both correspond to the relaxation of a vibrationally excited $N_2(V1)$ molecule, while electron impact vibrational excitation occurs from ground state N_2 molecules.

Comparing the characteristic relaxation times of VV and VT relaxation reveals that VT relaxation occurs on a significantly longer time scale than VV relaxation, i.e., 0.1 s vs 10^{-4} s. This long time scale of VT relaxation implies that this process only becomes significant when vibrational excitation occurs over a longer period of time, on the order of 0.1 s. As our plasma pulse is only in the microsecond range, it takes advantage of the long time scale of VT relaxation: switching off the power every 233 μs, as in our experiment, limits the rate of the slow VT relaxation, while fast reactions, like electron impact vibrational excitation and VV relaxation, already occur at this short time scale. This explains the high vibrational temperature and low gas temperature obtained in both our experiments and modeling.

4.1.c. Calculated (and Measured) VDFs. The strong population of the higher vibrational levels by electron impact vibrational excitation and VV relaxation, as well as the limited depletion of vibrational energy by VT relaxation in this short pulse, is also reflected in the vibrational distribution function (VDF) of N_2, calculated by the model, as illustrated in Figure 4 at five different times during the pulse (0, 1, 10, 100, and 233 μs) and in the afterglow (5 ms). As a reference, the Boltzmann distribution functions at the corresponding calculated gas temperature are also plotted with dashed lines in the same color, to indicate the degree of vibrational nonequilibrium. At 0 μs, the VDF exhibits a clear Boltzmann distribution with a temperature of 300 K, as indeed no power has been applied yet, so the gas is still in thermal equilibrium. As soon as the power is applied, all vibrational levels get highly populated within the first 1 μs of the pulse, almost instantly establishing the vibrational nonequilibrium that was observed in Figure 3. As the pulse progresses and more vibrational excitation takes place, the population of the higher vibrational levels raises further. As this occurs, the first eight vibrational levels of N_2 are populated enough to be observed in the Raman experiments. The experimental VDF, resulting from the vibrational population through the 233 μs pulse, is also shown in Figure 4 as green data points. Good agreement with the model is
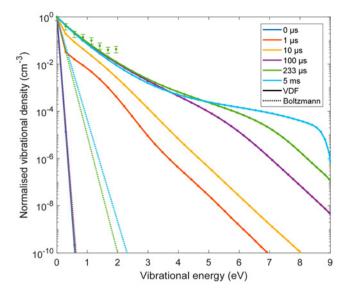

Figure 4. Calculated VDFs at five different times during the 233 μs pulse (0−233 μs) and in the afterglow (5 ms) (solid lines), as well as the Boltzmann distribution functions at the corresponding gas temperature (dashed lines), to indicate the strong degree of vibrational nonequilibrium. In addition, the measured VDF of the first eight vibrational energy levels at 233 μs is also shown (green data points).

achieved, especially for the lowest vibrational energy levels, showing the same excessive population of the vibrational levels in the plasma pulse as predicted by the model.

Even in the afterglow (5 ms), the population of the high vibrational levels is preserved (cf. the difference with the Boltzmann distributions). By this time, VV relaxation has almost equally populated all higher vibrational levels, while VT relaxation collisions with other N_2 molecules, as well as with N atoms, which are present to a great extent in the afterglow, have decreased the population of the lower vibrational levels. The VDF shows a characteristic plateau shape, which ultimately declines toward the highest vibrational levels, because of the low energy barrier for dissociation of these excited levels. This plateau shape thus indicates that even in the afterglow at the conditions under study, the N_2 molecules are constantly pumped toward the higher energy levels by VV relaxation, to eventually dissociate. This is highly beneficial for N_2 fixation, where the aim is to dissociate N_2 through this vibrational ladder climbing, being the most energy efficient dissociation process.

4.1.d. Calculated Electron Density and Temperature. As shown by the VDF in Figure 4, vibrational excitation already occurs to a great extent within the first μs of the pulse. During this first μs all MW power is focused in a small plasma volume, as the plasma is still igniting and expanding, resulting in a high power density. As shown by the evolution of the (self-consistently) calculated electron temperature and electron density in Figure 5, parts a and b, respectively, this high initial power density results in very fast rise in electron temperature and electron density during the first μs of the pulse. After this fast rise in electron density and peak in electron temperature, both properties are approximately constant through the pulse. The initially high electron density and temperature explain the fast electron kinetics from the very start of the pulse and the high vibrational excitation occurring upon plasma ignition. Figure 5 also shows that during the whole pulse the electron
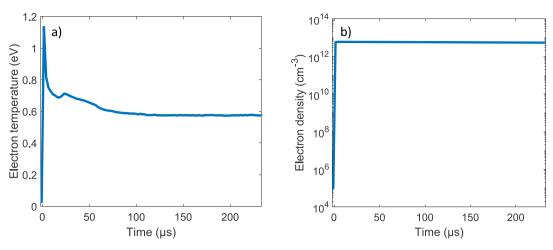
Figure 5. Time evolution of (a) the calculated electron temperature and (b) the calculated electron density through the 233 μs pulse.
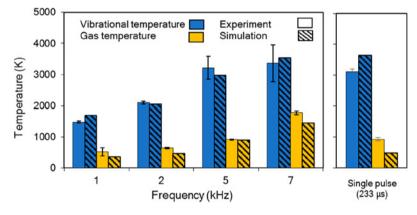

Figure 6. Measured and calculated vibrational and gas temperatures in the center (radial direction) of the plasma, spatially and time-averaged over the length of the pulse, for a pulsed MW plasma with a pulse width of 50 μs, at four different frequencies. As a reference, we also show the spatially averaged and time-averaged vibrational and gas temperatures for the isolated 233 μs pulse of the previous section.

temperature lies between 0.55 and 1.2 eV, which is found to be around the optimal electron temperature for electron impact vibrational excitation to occur.[8]

4.2. Repetitive Pulses: The Vibrational Nonequilibrium Depends on Pulse Frequency. *4.2.a. Vibrational and Gas Temperature.* While the single pulse experiment provides insights in the underlying mechanisms of vibrational nonequilibrium during power pulsing, its application potential for industrial N_2 fixation is unlikely. Indeed, pulsing the power at 30 Hz with a gas flow rate of 4 slm allows a large portion of the gas to pass through the reactor during the pulse off-time. Even if a high energy efficiency was achieved, the overall N_2 dissociation in the plasma would be limited. An obvious path is increasing the pulse frequency, so that more gas is processed by the plasma. However, it is not yet known to what extent the underlying mechanisms of the single pulse plasma are also applicable to these more relevant, higher pulse frequencies and how they change upon rising pulse frequencies. Therefore, using the knowledge of long scale VT relaxation processes being inhibited in an isolated pulse, we now investigate pulsed regimes of higher frequencies and reveal the influence of the pulse frequency on the vibrational nonequilibrium.

Figure 6 shows the vibrational and gas temperature, obtained from the Raman experiments and the simulations, for pulse frequencies of 1, 2, 5, and 7 kHz, with a 50 μs pulse width, a flow rate of 4 slm, and a pressure of 25 mbar. These values present the average temperature over the whole length

of the plasma in the radial center of the tube, where the laser is focused in the experimental setup. Similar to the modeling results of the single pulse, a correction factor is applied to the radially averaged temperatures of the 0D model, to account for the (hotter) center of the plasma (see Supporting Information). A reasonable agreement between experiments and simulations is achieved, indicating the same trend: as more pulses are applied in the same period of time, i.e. due to a higher frequency, more power is put into the plasma, which leads to more vibrational excitation and thus a higher vibrational temperature. However, the gas temperature also rises notably upon rising frequency, indicating that VT relaxation also gains significance. As a reference, the results of the isolated 233 μs pulse from previous section are also shown in Figure 8. However, it has to be noted that unlike the higher pulse regimes, the isolated pulse results only represent the temperature of a small portion of the gas, as the majority of the gas passes through the plasma tube in the pulse-off time.

The modeling results are displayed in more detail in Figure 7, which illustrates the calculated vibrational and gas temperature as a function of position, both inside and after the plasma column (which has a length of 5 cm), for the four different pulse frequencies (1, 2, 5, and 7 kHz) and a pulse width of 50 μs. These profiles show that the observed vibrational nonequilibrium arises from the vibrational temperature rising faster in every pulse through the plasma than the gas temperature. The vibrational temperature eventually
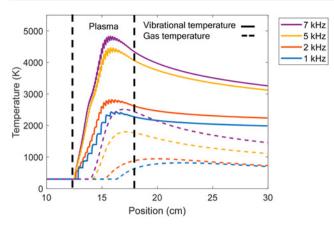
Figure 7. Calculated vibrational and gas temperature as a function of position, in a pulsed MW plasma of 50 μs pulse width, for four different pulse frequencies. The plasma length, which is equal to the width of the waveguide (cf. Figure 1), is 5 cm, and it is indicated by the vertical dashed lines.

reaches a maximum near the end of the plasma column, and at this point (or a bit earlier) the gas temperature starts to rise. Indeed, at this point, VT relaxation, which occurs on a longer time scale (cf. the single pulse results), becomes significant and gas heating occurs at the cost of vibrational energy. For higher pulse frequencies, the vibrational temperatures can reach a higher maximum. At the same time, however, VT relaxation occurs sooner in the plasma, resulting also in a higher overall gas temperature, as illustrated in Figures 6 and 7.

4.2.b. Underlying Mechanisms. The above results can again be explained from the time-integrated reaction rates of electron impact vibrational excitation, VV and VT relaxation, again summed over all 43 vibrational levels and multiplied with the energy difference of the transitions (cf. previous section), plotted in Figure 8 for the four different frequencies. A higher
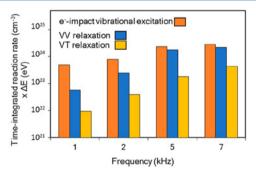

Figure 8. Time-integrated reaction rates of electron impact vibrational excitation, VV and VT relaxation, in a pulsed MW plasma with a pulse width of 50 μs, at four different frequencies, summed over all 43 vibrational levels and multiplied with the energy difference of the transitions.

pulse frequency yields higher reaction rates for all three vibrational processes, but the rise in VT rates is especially noticeable. Indeed, while the electron impact vibrational excitation rates and VV relaxation rates increase by about a factor 5 and 40, respectively, as the pulse frequency rises from 1 to 7 kHz, the VT relaxation rates increase by about a factor 4000. This is again explained by the characteristic time scale of the relaxation processes. Figure 9 shows the characteristic time scales of VV and VT relaxation for the four pulse frequencies,
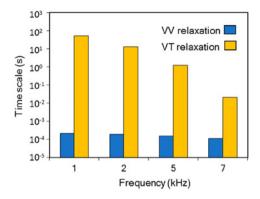

Figure 9. Time scale of VV and VT relaxation for 50 μs pulses at four different pulse frequencies at the experimental conditions (25 mbar), calculated using eqs 14 and 15 above.

calculated using eqs 14 and 15. The time scale of VT relaxation drops 4 orders of magnitude when the pulse frequency rises from 1 to 7 kHz, while the time scale of VV relaxation barely changes. As the time scale of VT relaxation is significantly reduced, more VT relaxation occurs in the μs pulses, resulting in more gas heating. As the rate coefficient of VT relaxation rises drastically upon rising temperature, even more VT relaxation occurs, yielding even higher gas heating (self-accelerating effect). This is in agreement with earlier computer simulations.[8]

Hence, a higher pulse frequency will yield a higher vibrational temperature, but also a higher gas temperature, due to more pronounced VT relaxation. Our experiments and calculations reveal that, at the conditions under study, a pulse frequency of 7 kHz will be unfavorable for the vibrational nonequilibrium in the plasma. In Table 3, we present the ratio

Table 3. Ratio between Measured Vibrational and Gas Temperature, for Four Different Pulse Frequencies, at a Pulse Width of 50 μs, Averaged over the Whole Plasma, as a Measure for the Degree of Vibrational Non-Equilibrium

1 kHz	2 kHz	5 kHz	7 kHz
2.2 ± 0.2	3.0 ± 0.2	3.7 ± 0.3	2.2 ± 0.2

between the measured vibrational and gas temperature as a measure for the nonequilibrium. Overall, at 5 kHz, the highest degree of nonequilibrium is achieved for the pulse width under study (50 μs), as it allows the gas to be exposed enough to the MW radiation to achieve high vibrational temperatures through vibrational excitation, and at the same time, the exposure is not too high for VT relaxation to significantly accelerate itself, as observed at 7 kHz.

4.2.c. Calculated (and Measured) VDFs. While the vibrational temperature serves as a good measure for the vibrational nonequilibrium, its definition in eq 1 does not include information about the population of the higher vibrational levels of N_2. To investigate the effect of the pulse frequency on the whole vibrational ladder, we present in Figure 10 the calculated VDFs at the last pulse of the plasma, for the four different pulse frequencies. Additionally, the measured VDFs of the vibrational levels that were sufficiently populated (i.e., above the detection limit) are also shown in the figure, as data points in the same color. Again these experimental VDFs display good agreement with the model for the lowest energy levels, and reasonable agreement for the higher levels. The
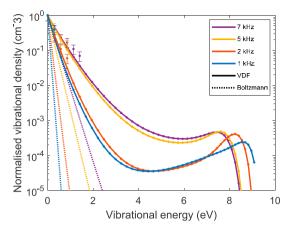
Figure 10. Calculated VDFs (solid lines), and measured VDFs (data points) in the last pulse of the plasma, for a pulse width of 50 μs, and four different pulse frequencies. In addition, the Boltzmann distribution functions at the corresponding gas temperatures (cf. Figure 7) are plotted in dashed lines, to indicate the strong degree of vibrational nonequilibrium.

Boltzmann distribution functions at the corresponding gas temperatures are also plotted with dashed lines in the same color. Both the experimental and calculated VDFs indicate a strong degree of vibrational nonequilibrium in all cases.

The pulse frequency affects the VDF in two ways. A higher pulse frequency leads to a generally higher population of all the vibrational states, which is beneficial to the vibrational nonequilibrium. However, at the same time, the maximum in the VDF at high vibrational energy, is shifted to somewhat lower vibrational energies. These two separate effects are a result of the higher reaction rates of both vibrational excitation and relaxation in the high pulse regime: Whereas electron impact vibrational excitation and VV relaxation deliver a high overall vibrational population, VT relaxation shifts the overpopulation toward lower levels in the vibrational ladder, by losing vibrational energy to gas heating, which is unfavorable for the vibrational nonequilibrium.

4.3. Repetitive Pulses: The Vibrational Nonequilibrium Depends on Pulse Width. *4.3.a. Vibrational and Gas Temperature.* Besides the pulse frequency, the pulse width also defines the amount of power applied to the plasma and will thus also affect the vibrational excitation. Figure 11 shows the vibrational and gas temperatures in the radial center and spatially averaged over the plasma length, obtained from the experiments and the simulations, for a pulse length of 10, 50, 200, and 400 μs, at a pulse frequency of 1 kHz, a flow rate of 4 slm and a pressure of 25 mbar. Again, a correction is applied to the radially averaged temperatures in the 0D model, to account for the hotter radial center (see Supporting Information). Even though the results in previous section revealed that 5 kHz gives better vibrational nonequilibrium, we selected a pulse frequency of 1 kHz. Indeed, unlike the 5 kHz regime, the 1 kHz pulse frequency allows us to explore pulse widths up to 400 μs without the risk of overheating the plasma equipment. The aim of this research is indeed to explore the separate effect of the pulse frequency and pulse width on the vibrational nonequilibrium in a wide range of conditions, rather than simply a parameter study to find the optimal conditions. Again, a reasonable agreement between simulations and experiments is reached, exhibiting the same trends. Similar to a higher pulse frequency, a longer pulse delivers both a higher vibrational and gas temperature. While barely any vibrational excitation or gas heating occurs in a 10 μs pulse, the 200 and 400 μs pulses demonstrate both a high vibrational and gas temperature.

This is illustrated in more detail in Figure 12, plotting the calculated vibrational and gas temperature as a function of position, for the four different pulse widths (10, 50, 200, and 400 μs). Similar to the temperature profiles in Figure 7, the vibrational temperature reaches a maximum as soon as VT relaxation becomes significant, and thus the gas temperature starts to rise. The effect of the pulse width is also very similar to that of the pulse frequency: a longer pulse results in a higher vibrational temperature but also in a higher gas temperature and a sooner rise of the latter, resulting in a more pronounced drop in vibrational temperature after its maximum is reached. These results indicate that similar to the pulse frequency, a longer pulse increases the significance of VT relaxation.

4.3.b. Underlying Mechanisms. The results are again explained by the calculated time-integrated reaction rates of electron impact vibrational excitation, VV and VT relaxation, summed over all 43 vibrational levels and multiplied with the energy difference of the transitions, plotted in Figure 13 for the different pulse widths. The longer pulses result in higher rates
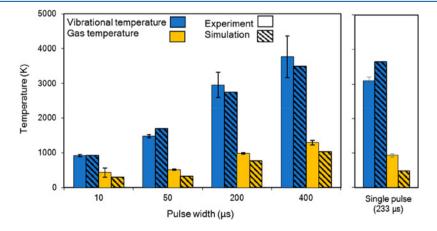

Figure 11. Measured and calculated vibrational and gas temperatures in the center (radial direction) of the plasma, spatially and time-averaged over the length of the pulse, for a pulsed MW plasma, at four different pulse widths and a pulse repetition frequency of 1 kHz. As a reference the spatially averaged and time-averaged vibrational and gas temperature is shown for the isolated 233 μs pulse.
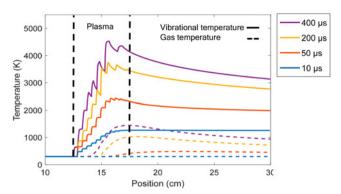
Figure 12. Calculated vibrational and gas temperature as a function of position, in a pulsed MW plasma, for a pulse frequency of 1 kHz and four different pulse widths. The plasma length, which is equal to the width of the waveguide (cf. Figure 1), is 5 cm, and is indicated by the vertical dashed lines.
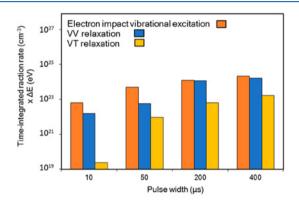

Figure 13. Time-averaged reaction rates of electron impact vibrational excitation, VV and VT relaxation, in a pulsed MW plasma, at four different pulse widths and a pulse repetition frequency of 1 kHz, summed over all 43 vibrational levels and multiplied with the energy difference of the transitions.

of all three vibrational mechanisms, but again the rate of VT relaxation rises more significantly. Indeed, the rates of electron impact excitation, VV relaxation and VT relaxation rise by a factor 30, 100 and 7000, respectively, when the pulse width rises from 10 to 400 μs.

Again the higher VT relaxation rates result from the shorter time scale of this process, as illustrated in Figure 14, for the
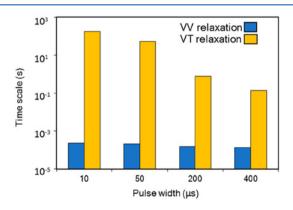

Figure 14. Time scale of VV and VT relaxation for a 1 kHz pulsed plasma at four different pulse widths, calculated using eqs 14 and 15 above.

four different pulse widths. Similar to the effect of the pulse frequency, when the pulse width rises from 10 to 400 μs, the time scale of VT relaxation drops by almost 4 orders of magnitude, while the time scale of VV relaxation barely changes. In addition, for the longer pulses, VT relaxation not only starts sooner (because of its shorter time scale), but also can occur for a longer time, inducing more significant gas heating, as illustrated in Figure 11.

The observed effects on the nonequilibrium can again be quantified by the ratio between the vibrational and gas temperature, shown in Table 4. It is clear that a pulsed MW

Table 4. Ratio between Vibrational and Gas Temperature for Four Different Pulse Widths, and a Pulse Repetition Frequency of 1 kHz, Averaged over the Whole Plasma, as a Measure for the Degree of Vibrational Non-Equilibrium

10 μs	50 μs	200 μs	400 μs
1.8 ± 0.2	2.4 ± 0.4	2.6 ± 0.5	2.5 ± 0.5

plasma with a pulse width of 200 or 400 μs does not provide significantly more pronounced nonequilibrium than a 50 μs pulse width. Indeed, although these longer pulses imply a longer excitation time for vibrational ladder climbing, the significant gas heating, and associated VT relaxation, compensate for the additional vibrational excitation. A pulsed MW plasma with 200 or 400 μs pulse width is thus considered less interesting from an energy-efficiency point of view, as it consumes four and eight times more power, respectively, than a 50 μs pulsed plasma at the same pulse frequency, but it does not display a significantly better vibrational nonequilibrium.

4.3.c. Calculated (and Measured) VDFs. The effect of the pulse width on the population of the vibrational levels is illustrated by the VDFs at the last pulse of the plasma in Figure 15, for the four different pulse widths (10, 50, 200, 400 μs) at a
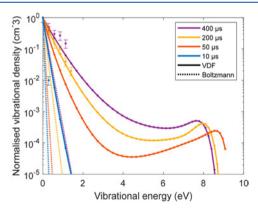

Figure 15. Calculated VDFs (solid lines) and measured VDFs (data points) in the last pulse of the plasma, for four different pulse widths and a pulse frequency of 1 kHz. In addition, the Boltzmann distribution functions at the corresponding gas temperatures (cf. Figure 11) are plotted in dashed lines, to indicate the strong degree of vibrational nonequilibrium.

pulse frequency of 1 kHz. Again, the measured VDFs of the vibrational levels that were populated above the detection limit are also shown in the figure as data points in the same color. Reasonable agreement is achieved, and in particular, the 200 μs regime is very well predicted by the model.

For every pulse width, the Boltzmann distribution function at the corresponding gas temperature is again plotted with a dashed line in the same color. The VDFs show a stronger vibrational excitation upon increasing pulse width, yielding a very pronounced nonequilibrium, and strong overpopulation for the higher vibrational levels compared to the Boltzmann distributions, in the 50, 200, and 400 μs pulse regimes. The 10 μs pulse width, however, is too short to significantly excite the higher vibrational levels. Similar to the pulse frequency, two effects are observed upon rising pulse width: longer pulses result in a higher population of all vibrational levels due to the higher electron impact vibrational excitation and VV relaxation, but the overpopulation is shifted away from the highest energy levels, due to the significant role of VT relaxation.

4.4. The Energy Efficiency of Power Pulsing. In the previous sections, we demonstrated how power pulsing is able to deliver a pronounced vibrational nonequilibrium, which is important for energy-efficient N_2 dissociation. This vibrational nonequilibrium is achieved within very short periods of time, meaning that overall little power is consumed. For the 50 μs pulses at 5 kHz, which yielded the highest nonequilibrium in our study, only 100 W is required to reach a vibrational temperature of 3200 K at a gas temperature of 900 K. To demonstrate the energy efficiency of the power pulsing effect, we compare this case to a continuous plasma at similar conditions. Gatti et al.[53] operated a continuous pure N_2 plasma in a very similar setup, using a plasma tube of the same size at a pressure of 17 mbar, a flow rate of 7.8 slm and power of 130 W. These conditions provide a specific energy input (SEI) of 0.22 eV/molecule,[53] which is comparable to the SEI of 0.32 eV/molecule of the 5 kHz regime in our study. These similar conditions report higher values for both vibrational and gas temperature (i.e., 4700 and 2000 K, respectively), but a less pronounced vibrational nonequilibrium. Indeed, in the center of the plasma, the ratio of the vibrational and gas temperature, which we use as a quantification of the vibrational non-equilibrium, is reported to be 2.2 ± 0.6, while in our case at 5 kHz, a value of 3.7 ± 0.3 is obtained (cf. Table 3). Hence, the ratio of the vibrational and gas temperature (as a measure for the vibrational nonequilibrium) is almost twice as high in our pulsed regime than in a continuous regime, for a comparable SEI input, which demonstrates the efficiency of power pulsing for reaching a pronounced vibrational nonequilibrium.

5. CONCLUSION

We investigated the vibrational nonequilibrium in a N_2 pulsed MW plasma at 25 mbar, which may be used for energy-efficient plasma-based N_2 fixation as a potential green alternative to the Haber—Bosch process. We measured the vibrational and gas temperatures by vibrational Raman spectroscopy, and compared the results with a 0D chemical kinetics model, describing all N_2 vibrational levels up to the dissociation limit, as well as self-consistent gas heating. By conducting both an experimental and computational study we are able to analyze the behavior of the gas and vibrational temperature on a μs time scale through Raman spectroscopy, while also presenting the modeled vibrational dynamics, which are not accessible through experiments. Using the model, we were able to explain the experimental results, based on the rates and time scales of the three main vibrational mechanisms and the calculated VDFs. Reasonable agreement was reached between the measured and calculated vibrational and gas temperatures,

for different pulse frequencies and widths. The aim was to explore the potential of plasma pulsing, to prevent the plasma from excessive gas heating, and thus to sustain a favorable vibrational nonequilibrium.

We showed that a pulsed plasma takes advantage of the different time scales on which the three major vibrational mechanisms occur, i.e., electron impact vibrational excitation, VV and VT relaxation. VT relaxation, which heats up the plasma, leading to energy losses, can be reduced upon pulsing, because it operates on a longer time scale than the vibrational mechanisms that favor the nonequilibrium, i.e., electron impact vibrational excitation, and VV relaxation. As shown by the calculated VDFs, plasma pulsing can very quickly populate the high N_2 vibrational levels, sustaining a pronounced non-equilibrium over the whole vibrational ladder.

The advantage of pulsing is, however, diminished for too high pulse frequency (around 7 kHz) or pulse width (above 400 μs) at the conditions under study. While these conditions still delivered a clear vibrational nonequilibrium, no significant benefits were revealed compared to the other, less power-demanding and thus more energy-efficient regimes. At these conditions, the power is supplied either too frequently or for too long time, so that the long time scale VT relaxation is no longer inhibited, thus inducing more gas heating. This yields a significant loss of vibrational energy, and thus it results in less pronounced vibrational nonequilibrium, which will lead to less energy-efficient N_2 dissociation. A balance in pulse frequency and pulse length was reached at 5 kHz and 50 μs, at which vibrational excitation occurs excessively, populating the higher vibrational levels, while gas heating is limited, reaching a vibrational temperature of 3200 K, with a gas temperature of only 900 K. In this regime, the vibrational excitation efficiency was maximized.

As these conditions show a very promising vibrational nonequilibrium, while only requiring a limited power-on time, pulsed plasmas do seem very interesting for energy-efficient vibrational excitation. Furthermore, from this work, we understand the underlying dynamics for vibrational excitation during power pulsing and how basic pulse parameters can be changed to manipulate these dynamics and maximize the excitation efficiency. These insights are very interesting to further explore and optimize power pulsing for plasma-based N_2 fixation.

■ ASSOCIATED CONTENT

ⓢ Supporting Information

The Supporting Information is available free of charge on the ACS Publications website at DOI: 10.1021/acs.jpcc.9b06053.

> Reactions included in the model as well as their rate coefficients or cross sections, the calculation of the power density as input for the 0D model based on plasma images, a sensitivity analysis of the most important approximations made in the 0D model, the Raman spectra and power profile of the single pulse experiment at 10, 30, 60, 200, and 400 μs, and the Raman spectra and power profiles of the repetitive pulse experiments 30 μs after the start of the pulse (PDF)

■ AUTHOR INFORMATION

Corresponding Author

*(A.B.) E-mail: annemie.bogaerts@uantwerpen.be.

ORCID ◉
S. Van Alphen: 0000-0003-0870-1453
V. Vermeiren: 0000-0002-6201-2977
A. Bogaerts: 0000-0001-9875-6460

Notes
The authors declare no competing financial interest.

■ REFERENCES

(1) Patil, B. S.; Wang, Q.; Hessel, V.; Lang, J. Plasma N2-Fixation: 1900−2014. *Catal. Today* **2015**, *256*, 49−66.

(2) Canfield, D. E.; Glazer, A. N.; Falkowski, P. G. The Evolution and Future of Earth's Nitrogen Cycle. *Science (Washington, DC, U. S.)* **2010**, *330*, 192−196.

(3) Cherkasov, N.; Ibhadon, A. O.; Fitzpatrick, P. A Review of the Existing and Alternative Methods for Greener Nitrogen Fixation. *Chem. Eng. Process.* **2015**, *90*, 24−33.

(4) Galloway, J. N. The Global Nitrogen Cycle: Changes and Consequences. *Environ. Pollut.* **1998**, *102*, 15−24.

(5) Tanabe, Y.; Nishibayashi, Y. Developing More Sustainable Processes for Ammonia Synthesis. *Coord. Chem. Rev.* **2013**, *257*, 2551−2564.

(6) Anastasopoulou, A.; Wang, Q.; Hessel, V.; Lang, J. Energy Considerations for Plasma-Assisted N-Fixation Reactions. *Processes* **2014**, *2*, 694−710.

(7) Patil, B. S.; Cravotto, G.; Bonrath, W.; Hessel, V.; Fitzpatrick, P.; Lang, J. Industrial Applications of Plasma, Microwave and Ultrasound Techniques: Nitrogen-Fixation and Hydrogenation Reactions. *Chem. Eng. Process.* **2013**, *71*, 19−30.

(8) Wang, W.; Patil, B.; Heijkers, S.; Hessel, V.; Bogaerts, A. Nitrogen Fixation by Gliding Arc Plasma: Better Insight by Chemical Kinetics Modelling. *ChemSusChem* **2017**, *10*, 2110.

(9) Bogaerts, A.; Kozák, T.; van Laer, K.; Snoeckx, R. Plasma-Based Conversion of CO₂: Current Status and Future Challenges. *Faraday Discuss.* **2015**, *183*, 217−232.

(10) Asisov, R. I.; Givotov, V. K.; Rusanov, V. D.; Fridman, A. High Energy Chemistry (Khimia Vysokikh Energij). *Sov. Phys.* **1980**, *14*, 366.

(11) Bogaerts, A.; Neyts, E. C. Plasma Technology: An Emerging Technology for Energy Storage. *ACS Energy Lett.* **2018**, *3*, 1013−1027.

(12) Hong, J.; Aramesh, M.; Shimoni, O.; Seo, D. H.; Yick, S.; Greig, A.; Charles, C.; Prawer, S.; Murphy, A. B. Plasma Catalytic Synthesis of Ammonia Using Functionalized-Carbon Coatings in an Atmospheric-Pressure Non-Equilibrium Discharge. *Plasma Chem. Plasma Process.* **2016**, *36*, 917−940.

(13) Cotrino, J.; González-Elipe, A. R.; Montoro-Damas, A. M.; Lambert, R. M.; Gómez-Ramírez, A. About the Enhancement of Chemical Yield during the Atmospheric Plasma Synthesis of Ammonia in a Ferroelectric Packed Bed Reactor. *Plasma Processes Polym.* **2017**, *14*, 1600081.

(14) Gómez-Ramírez, A.; Cotrino, J.; Lambert, R. M.; González-Elipe, A. R. Efficient Synthesis of Ammonia from N2 and H2 alone in a Ferroelectric Packed-Bed DBD Reactor. *Plasma Sources Sci. Technol.* **2015**, *24*, 065011.

(15) Patil, B. S. *Plasma (Catalyst) − Assisted Nitrogen Fixation: Reactor Development for Nitric Oxide and Ammonia Production*; Ph.D. Thesis, TU/e Eindhoven Institute of Technology: 2017.

(16) Mizushima, T.; Matsumoto, K.; Sugoh, J. I.; Ohkita, H.; Kakuta, N. Tubular Membrane-like Catalyst for Reactor with Dielectric-Barrier- Discharge Plasma and Its Performance in Ammonia Synthesis. *Appl. Catal., A* **2004**, *265*, 53−59.

(17) Bai, M.; Wang, N.; Zhang, Z.; Bai, M.; Bai, X. Plasma Synthesis of Ammonia with a Microgap Dielectric Barrier Discharge at Ambient Pressure. *IEEE Trans. Plasma Sci.* **2003**, *31*, 1285−1291.

(18) Kim, H. H.; Teramoto, Y.; Ogata, A.; Takagi, H.; Nanba, T. Atmospheric-Pressure Nonthermal Plasma Synthesis of Ammonia over Ruthenium Catalysts. *Plasma Processes Polym.* **2017**, *14*, 1600157.

(19) Akay, G.; Zhang, K. Process Intensification in Ammonia Synthesis Using Novel Coassembled Supported Microporous Catalysts Promoted by Nonthermal Plasma. *Ind. Eng. Chem. Res.* **2017**, *56*, 457−468.

(20) Iwamoto, M.; Akiyama, M.; Aihara, K.; Deguchi, T. Ammonia Synthesis on Wool-Like Au, Pt, Pd, Ag, or Cu Electrode Catalysts in Nonthermal Atmospheric-Pressure Plasma of N2 and H2. *ACS Catal.* **2017**, *7*, 6924−6929.

(21) Peng, P.; Li, Y.; Cheng, Y.; Deng, S.; Chen, P.; Ruan, R. Atmospheric Pressure Ammonia Synthesis Using Non-Thermal Plasma Assisted Catalysis. *Plasma Chem. Plasma Process.* **2016**, *36*, 1201−1210.

(22) Partridge, W. S.; Parlin, R. B.; Zwolinski, B. J. Fixation of Nitrogen in a Crossed Discharge. *Ind. Eng. Chem.* **1954**, *46*, 1468−1471.

(23) Akiyama, H.; Hackam, R.; Okamoto, K.; Namihira, T.; Katsuki, S. Production of Nitric Oxide Using a Pulsed Arc Discharge. *IEEE Trans. Plasma Sci.* **2002**, *30*, 1993−1998.

(24) Mutel, B.; Dessaux, O.; Goudmand, P. Energy Cost Improvement of The Nitrogen Oxides Synthesis in a Low Pressure Plasma. *Rev. Phys. Appl.* **1984**, *19*, 461−464.

(25) Krop, J.; Pollo, I. Chemical Reactors for Synthesis of Nitrogen Oxide in a Stream of Low-Temperature Plasma. III. Reactor to Freeze Reaction Products by Injection of Water. *Chemia* **1981**, *678*, 51−59.

(26) Coudert, J. F.; Baronnet, J. M.; Rakowitz, J.; Fauchais, P. Synthesis of Nitrogen Oxides in a Plasma Produced by a Jet Arc Generator. In *Symp. Int. Chim. Plasmas*; Fauchais, P., Ed.; 1977.

(27) Patil, B. S.; Cherkasov, N.; Lang, J.; Ibhadon, A. O.; Hessel, V.; Wang, Q. Low Temperature Plasma-Catalytic NOxsynthesis in a Packed DBD Reactor: Effect of Support Materials and Supported Active Metal Oxides. *Appl. Catal., B* **2016**, *194*, 123−133.

(28) Lane, J.; Hughes, D.; Schoenbach, K. H.; Heller, R.; Jiang, C.; Malik, M. A. Ozone-Free Nitric Oxide Production Using an Atmospheric Pressure Surface Discharge − A Way to Minimize Nitrogen Dioxide Co-Production. *Chem. Eng. J.* **2016**, *283*, 631−638.

(29) Polak, L. S.; Ovsiannikov, A. A.; Slovetsky, D. I.; Vurzel, F. B. *Theoretical and Applied Plasma Chemistry*; Nauka (Science): Moscow, 1975.

(30) Lang, J.; Hessel, V.; Medrano, J. A.; van Rooij, G. J.; Peeters, F. J. J.; Patil, B. S.; Gallucci, F.; Wang, Q. Plasma Assisted Nitrogen Oxide Production from Air: Using Pulsed Powered Gliding Arc Reactor for a Containerized Plant. *AIChE J.* **2018**, *64*, 526−537.

(31) Rahman, M.; Cooray, V. NOx Generation in Laser-Produced Plasma in Air as a Function of Dissipated Energy. *Opt. Laser Technol.* **2003**, *35*, 543−546.

(32) Birkeland, K. On the Oxidation Af Atmospheric Nitrogen in Electric Arcs. *Trans. Faraday Soc.* **1906**, *2*, 98−116.

(33) Shmelev, V. M.; Saveliev, A. V.; Kennedy, L. A. Plasma Chemical Reactor with Exploding Water Jet. *Plasma Chem. Plasma Process.* **2009**, *29*, 275−290.

(34) Bian, W.; Song, X.; Shi, J.; Yin, X. Nitrogen Fixed into HNO 3 by Pulsed High Voltage Discharge. *J. Electrost.* **2012**, *70*, 317−326.

(35) Rehbein, N.; Cooray, V. NOx Production in Spark and Corona Discharges. *J. Electrost.* **2001**, *51−52*, 333−339.

(36) Kim, T.; Song, S.; Kim, J.; Iwasaki, R. Formation of NOx from Air and N2/O2Mixtures Using a Nonthermal Microwave Plasma System. *Jpn. J. Appl. Phys.* **2010**, *49*, 126201.

(37) Patil, B. S.; Rovira Palau, J.; Hessel, V.; Lang, J.; Wang, Q. Plasma Nitrogen Oxides Synthesis in a Milli-Scale Gliding Arc

Reactor: Investigating the Electrical and Process Parameters. *Plasma Chem. Plasma Process.* **2016**, *36*, 241−257.

(38) Berthelot, A.; Bogaerts, A. Modeling of CO_2 Splitting in a Microwave Plasma: How to Improve the Conversion and Energy Efficiency. *J. Phys. Chem. C* **2017**, *121*, 8236−8251.

(39) Snoeckx, R.; Bogaerts, A. Plasma Technology − a Novel Solution for CO_2 Conversion? *Chem. Soc. Rev.* **2017**, *46*, 5805−5863.

(40) Wang, Q.; Patil, B.; Anastasopoulou, A.; Butala, S.; Rovira, J.; Hessel, V.; Lang, J. Plasma Assisted Nitrogen Fixation Process. *22nd Int. Symp. Plasma Chem.* **2015**, 1−2.

(41) Asisov, R. I.; Vakar, A. K.; Jivitov, V. K.; Krotov, M. F.; Zinoviev, O. A.; Potapkin, B. V.; Rusanov, A. A.; Rusanov, V. D.; Fridman, A. A. Non-Equilibrium Plasma-Chemical Process of CO2 Decomposition in a Supersonic Microwave Discharge. *Proc. USSR Acad. Sci.* **1983**, *271*, 94−97.

(42) Vermeiren, V.; Bogaerts, A. Supersonic Microwave Plasma: Potential and Limitations for Energy-Efficient CO2 Conversion. *J. Phys. Chem. C* **2018**, *122*, 25869−25881.

(43) Vermeiren, V.; Bogaerts, A. Improving the Energy Efficiency of CO2 Conversion in Non-Equilibrium Plasmas through Pulsing. *J. Phys. Chem. C* **2019**, *123*, 17650.

(44) Silva, T.; Britun, N.; Godfroid, T.; Snyders, R. Optical Characterization of a Microwave Pulsed Discharge Used for Dissociation of CO2. *Plasma Sources Sci. Technol.* **2014**, *23*, 025009.

(45) van den Bekerom, D. C. M.; Linares, J. M. P.; Verreycken, T.; van Veldhuizen, E. M.; Nijdam, S.; Bongers, W.; Van de Sanden, R.; Van Rooij, G. J. The Importance of Thermal Dissociation in CO2Microwave Discharges Investigated by Power Pulsing and Rotational Raman Scattering. *Plasma Sources Sci. Technol.* **2019**, *28*, 055015.

(46) Britun, N.; Silva, T.; Chen, G.; Godfroid, T.; Van Der Mullen, J.; Snyders, R. Plasma-Assisted CO2 Conversion: Optimizing Performance via Microwave Power Modulation. *J. Phys. D: Appl. Phys.* **2018**, *51*, 144002.

(47) Massabieaux, B.; Gousset, G.; Lefebvre, M.; Pealat, M. Determination of N2(X) Vibrational Level Populations and Rotational Temperatures Using CARS in a D.C. Low Pressure Discharge. *J. Phys. (Paris)* **1987**, *48*, 1939.

(48) Capitelli, M.; Gorse, C.; Ricard, A. Non Equilibrium Dissociation and Ionization of N2 in Decaying Plasmas. *J. Phys., Lett.* **1982**, *43*, 417.

(49) Macko, P.; Cunge, G.; Sadeghi, N. Density of N 2 (X1 Σ G ; v = 18) Molecules in a Dc Glow Discharge Measured by Cavity Ringdown Spectroscopy at 227 Nm. *J. Phys. D: Appl. Phys.* **2001**, *34*, 1807−1811.

(50) Guerra, V.; Sa, P. A.; Loureiro, J. Nitrogen Pink Afterglow: The Mystery Continues Nitrogen Pink Afterglow: The Mystery Continues. *J. Phys.: Conf. Ser.* **2007**, *63*, No. 012007.

(51) Bruggeman, P. J.; Sadeghi, N.; Schram, D. C.; Linss, V. Gas Temperature Determination from Rotational Lines in Non-Equilibrium Plasmas: A Review. *Plasma Sources Sci. Technol.* **2014**, *23*, 023001.

(52) Herzberg, G. *Molecular Spectra and Molecule Structure. I. Diatomic Molecules*; New York, 1940.

(53) Gatti, N.; Ponduri, S.; Peeters, F.; van den Bekerom, D. C. M.; Minea, T.; Tosi, P.; Van de Sanden, R.; Van Rooij, G. J. Preferential Vibrational Excitation in Microwave Nitrogen Plasma Assessed by Raman Scattering. *Plasma Sources Sci. Technol.* **2018**, *27*, 055006.

(54) Simek, M.; Ambrico, P. F.; Prukner, V. LIF Study of N 2 (A3Σ,v = 0 − 10) Vibrational Kinetics under Nitrogen Streamer Conditions. *J. Phys. D: Appl. Phys.* **2015**, *48*, 265202.

(55) van den Bekerom, D. *Vibrational Excitation for Efficient Chemistry in CO2Microwave Plasmas*; Technische Universiteit Eindhoven; 2018.

(56) Pancheshnyi, S.; Eismann, B.; Hagelaar, G. J. M.; Pitchford, L. C. Computer code ZDPlasKin, http://www.zdplaskin.laplace.univ-tlse.fr (University of Toulouse, LAPLACE, CNRS-UPSINP: Toulouse, France, 2008).

(57) Hagelaar, G. J. M.; Pitchford, L. C. Solving the Boltzmann Equation to Obtain Electron Transport Coefficients and Rate Coefficients for Fluid Models. *Plasma Sources Sci. Technol.* **2005**, *14*, 722−733.

(58) IST-Lisbon database, www.lxcat.net, retrieved in February 2018.

(59) Phys4entry database, CNR IMIP Bari and SER&Practices, retrieved in February 2019.

(60) Colonna, G.; Laporta, V.; Celiberto, R.; Capitelli, M.; Tennyson, J. Non-Equilibrium Vibrational and Electron Energy Distributions Functions in Atmospheric Nitrogen Ns Pulsed Discharges and Ms Post-Discharges: The Role of Electron Molecule Vibrational Excitation Scaling-Laws. *Plasma Sources Sci. Technol.* **2015**, *24*, 035004.

(61) Saxena, S. C.; Chen, S. H. P. Thermal Conductivity of Nitrogen in the Temperature Range 350−2500 K. *Mol. Phys.* **1975**, *29*, 1507−1519.

(62) Heijkers, S.; Snoeckx, R.; Kozák, T.; Silva, T.; Godfroid, T.; Britun, N.; Snyders, R.; Bogaerts, A. CO_2 Conversion in a Microwave Plasma Reactor in the Presence of N_2: Elucidating the Role of Vibrational Levels. *J. Phys. Chem. C* **2015**, *119*, 12815−12828.

(63) Adamovich, I. V.; MacHeret, S. O.; Rich, J. W.; Treanor, C. E. Vibrational Energy Transfer Rates Using a Forced Harmonic Oscillator Model. *J. Thermophys. Heat Transfer* **1998**, *12*, 57−65.